# Geant4 simulations of x-ray photon pileup produced by runaway electrons in streamer discharges

Cite as: Phys. Plasmas **29**, 053506 (2022); https://doi.org/10.1063/5.0086579 Submitted: 27 January 2022 • Accepted: 16 April 2022 • Published Online: 09 May 2022

J. G. Pantuso, (D) C. L. da Silva, J. T. Sanchez, et al.











# Geant4 simulations of x-ray photon pileup produced by runaway electrons in streamer discharges

Cite as: Phys. Plasmas **29**, 053506 (2022); doi: 10.1063/5.0086579 Submitted: 27 January 2022 · Accepted: 16 April 2022 · Published Online: 9 May 2022







J. G. Pantuso, <sup>1</sup> C. L. da Silva, <sup>1,a)</sup> id J. T. Sanchez, <sup>1</sup> and G. S. Bowers<sup>2</sup>

### **AFFILIATIONS**

Department of Physics and Langmuir Lab, New Mexico Tech, Socorro, New Mexico 87801, USA

#### **ABSTRACT**

Runaway electron acceleration is the keystone process responsible for the production of energetic radiation by lightning and thunderstorms. In the laboratory, it remains undetermined if runaway electrons are merely a consequence of high electric fields produced at the ionization fronts of electrical discharges, or if they impact the discharge formation and propagation. In this work, we simulate photon pileup in a detector next to a spark gap. We compare laboratory measurements to ensembles of monoenergetic electron beam simulations performed with Geant4 (using the Monte Carlo method). First, we describe the x-ray emission properties of monoenergetic beams with initial energies in the 20 to 75 keV range. Second, we introduce a series of techniques to combine monoenergetic beams to produce general-shape electron energy spectra. Third, we proceed to attempt to fit the experimental data collected in the laboratory, and to discuss the ambiguities created by photon pileup and how it constrains the amount of information that can be inferred from the measurements. We show that pileup ambiguities arise from the fact that every single monoenergetic electron beam produces photon deposited energy spectra of similar qualitative shape and that increasing the electron count in any beam has the same qualitative effect of shifting the peak of the deposited energy spectrum toward higher energies. The best agreement between simulations and measurements yields a mean average error of 8.6% and a R-squared value of 0.74.

Published under an exclusive license by AIP Publishing. https://doi.org/10.1063/5.0086579

# I. INTRODUCTION

Research on the role of runaway electrons in transient plasma discharges in the laboratory<sup>1-4</sup> and nature<sup>5-7</sup> has bloomed in recent years. The basic idea of how runaway electrons emerge is simple.8 When an electric field is applied to air, a free electron begins to accelerate. The electron interacts with air molecules, loses energy due to numerous types of collisions, and decelerates. The effects of these collisions can be represented by an energydependent effective friction force, as shown in Fig. 1(a). If the field supplies more energy to the electron than is lost due to collisions, the electron may enter the runaway state. 9,10 This phenomenon happens for energies larger than 100 eV, where the friction force experienced by electrons decreases with increasing electron energy [marked by a red circle in Fig. 1(a)]. More precisely, in the energy range between 300 eV and 300 keV, the runaway electron threshold energy (in eV) can be approximated by the following formula  $K_{th}$  $= 8.4 \times 10^5 E^{-1.4}$ , where E is the applied electric field in kV/cm.

This formula is obtained by fitting the effective friction force as given by Berger et al., 11 and it corresponds to sea-level atmospheric pressure. The Kth approximation is shown as an orange dashed curve in Fig. 1(a). In order to begin a runaway event (which may grow to become a runaway electron avalanche<sup>12</sup>), a highenergy ( $>K_{\rm th}$ ) seed electron is necessary.<sup>7,9</sup> For instance for E = 12.5 kV/cm,  $K_{\text{th}} = 23 \text{ keV}$ , as marked in Fig. 1(a) with a triangle. This high-energy seed electron can actually come from a variety of sources, including cosmic background radiation, 12 other high-energy electrons produced via positron and gamma-ray feedback effects, 13 or low-energy electrons accelerated by the electric field produced at streamer ionization fronts. 9,14 When electrons are pushed into the runaway state [i.e., over the "hill" in Fig. 1(a)] by the very high electric field at streamer tips, the process is known as the thermal (or cold) runaway mechanism.  $^{10,\hat{15},16}$  The thermal runaway electron mechanism is further supported by Monte Carlo simulations and laboratory spark investigations. 1,1

<sup>&</sup>lt;sup>2</sup>Los Alamos National Laboratory, Los Alamos, New Mexico 87545, USA

a) Author to whom correspondence should be addressed: caitano.dasilva@nmt.edu

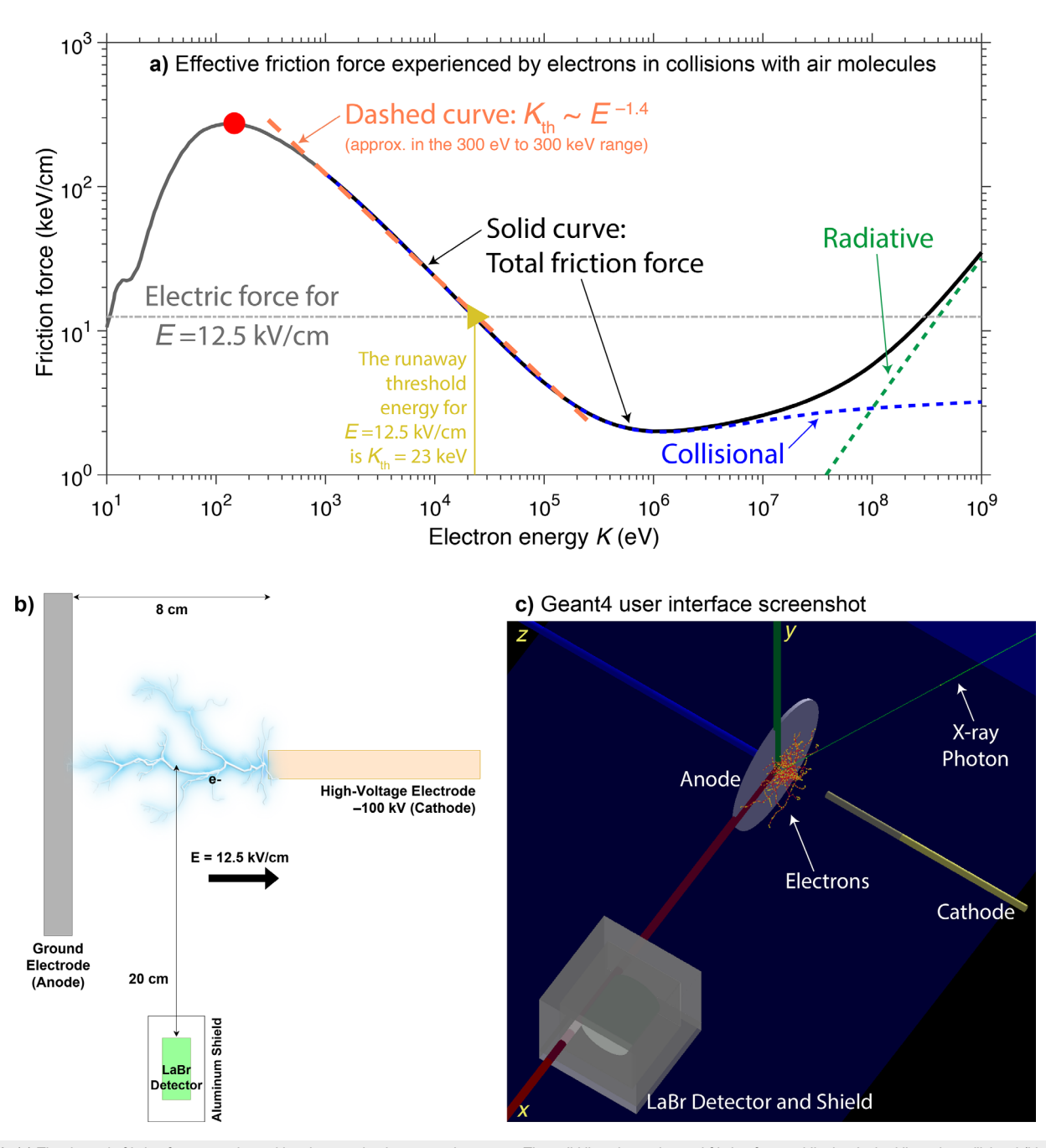


**FIG. 1.** (a) The dynamic friction force experienced by electrons in air at ground pressure. The solid line shows the total friction force, while the dashed lines the collisional (blue) and radiative (green) contribution. The horizontal dot-dashed line shows the applied electric force corresponding to an electric field of 12.5 kV/cm. The intersection between both curves (marked with a triangle) defines the runaway threshold energy for this electric field value (which is 23 keV). For low energies, the data in the figure come from the widely referenced ICRU Report 37<sup>18</sup> (their Fig. 8.2), while for energies  $\geq$  1 keV we use the more recent NIST database. Panel (a) also shows the  $K_{th}(E)$  approximation discussed in the text as an orange dashed curve. (b) Schematic representation of the experimental setup simulated. (c) Screenshot of Geant4's graphical interface. The copper cathode is the yellow rod, the aluminum anode is the white disk, and the LaBr<sub>3</sub>:Ce x-ray detector is the cylinder inside an aluminum shielding box. The red lines show electron paths, while the green ones photon paths.

When electrons in a runaway state approach the nucleus of the background gas molecules they change their velocity and emit Bremsstrahlung x-ray radiation, <sup>19</sup> which allows researchers to remotely probe the physics of this phenomenon.<sup>6</sup> In the early 2000s,

work by Moore,<sup>20</sup> Dwyer,<sup>21</sup> and colleagues showed that lightning produces x-rays from several keV to many MeV. Since then, substantial progress has been made toward connecting the measured x-ray emissions with the properties of runaway electrons emitted by lightning

leader tips, <sup>22–25</sup> but a long road still lies ahead of the atmospheric electricity community to fully probe the energy distribution of runaway electrons emitted by lightning and their dependence on the lightning channel properties. Lightning is a short-lived, stochastic, and dangerous phenomenon, making it challenging to study in close proximity. For these reasons, researchers have relied heavily on laboratory experiments to understand energetic electron and photon production by electrical discharges. <sup>1,4,17,26–39</sup>

Laboratory experiments have revealed that runaway electrons can be readily produced in short laboratory discharges under applied voltages of the order of  $-100\,\mathrm{kV}$ . These experiments have revealed that a number of factors can be adjusted to increase the flux of runaway electrons (or their current), including the use of higher applied voltages (or more precisely, average electric fields in the gap), faster voltage risetimes, lower gas pressures, gasses with lower molecular mass, cathodes made of materials with higher work functions (for voltage pulse risetimes longer than 1 ns), and anodes made of materials with higher atomic numbers.<sup>40</sup> Investigations with laboratory discharges allow researchers to repeat the "miniaturized lightning flash" multiple times and provide statistical inferences about runaway electron production and subsequent x-ray emissions. For instance, da Silva et al. showed that runaway electrons and their associated x-ray emissions are prolifically produced in an 8-cm-long, rod-to-plane gap under an applied voltage of  $-100 \, \text{kV}$ . These authors inferred that median x-ray burst energies varied between 33 and 96 keV, depending on the observation geometry, type of anode, and type of filter placed between the source and x-ray detector. These authors also inferred that the discharges produced between  $5 \times 10^4$  and  $0.5 \times 10^6$  runaway electrons and that the x-ray emissions were produced when runaway electrons collided with the anode.

In this paper, we simulate photon pileup in a detector near a spark gap. We do so by simulating monoenergetic runaway electron beams in atmospheric pressure air under an applied electric field of 12.5 kV/cm, imitating the experimental setup used by da Silva *et al.*<sup>1</sup> Using Geant4, we calculate the expected behavior of the x-ray emissions from electron beams with initial kinetic energy between 20 and 75 keV. A key point of this article is the introduction of algebraic tools that allow us to create general-shape electron energy spectra by combining previously simulated monoenergetic beams. Finally, we use the simulations to understand the ambiguities created by photon pileup at the x-ray detector, which is a natural consequence of performing close-range x-ray observations of electrical discharges. We conclude by discussing avenues to circumvent pileup ambiguities when inferring the energy spectrum of the source runaway electrons.

# II. METHODOLOGY

#### A. Geant4 simulation setup

In this work, we use the Geant4 (Geometry and Tracking) object-oriented C ++ toolkit, which utilizes Monte Carlo techniques to simulate the complex interactions between a wide variety of particles and a background medium. 41–43 Of particular interest to our project is Geant4's capability of tracking individual photons. This process can be computationally intensive and time-consuming but allows us to almost totally circumvent the issues associated with photon pileup—at least within the modeling efforts. Geant4 has already been successfully used to simulate runaway electrons in the past. 44–46 Here, runaway electrons are assumed to be formed by the thermal runaway acceleration

mechanism in compact regions of strong electric fields ahead of streamer tips.  $^{9,15}$  We start the simulations when the streamer ionization fronts are 2 cm away from the ground electrode. We assume that the runaway electrons can be modeled as a series of monoenergetic beams, with initial energies between 20 and 75 keV. The underlying assumption here is that when streamers are close to the ground electrode, the runaway electrons detach from the streamer ionization front and propagate under the applied average gap field, which is  $12.5 \, \text{kV/cm}$  in this case. The minimum initial energy value of  $20 \, \text{keV}$  is just under the threshold runaway value  $K_{th}$  for the average gap field [marked in Fig. 1(a) with a triangle]. The maximum initial energy value of  $75 \, \text{keV}$  is the potentially maximum energy gain from the externally applied voltage (=  $12.5 \, \text{kV/cm} \times 6 \, \text{cm}$ ) before the start of the simulation tracking. The simulation setup is schematically shown in Fig. 1(b).

The Geant4 simulation starts with electrons released 2 cm away from the ground electrode (anode in the figure); they accelerate under an applied 12.5 kV/cm electric field and experience a series of collisions with air molecules, modeled with the Monte Carlo stochastic simulation approach. In this small-scale setup, electrons produce bremsstrahlung x-rays when they collide with the anode (a disk with 10 cm diameter and 2.5 mm thick), as verified by our simulations. Photons are detected by an accurate mass model of a Saint Gobain LaBr<sub>3</sub>:Ce scintillation detector positioned 20 cm away, as shown in Fig. 1(b). The detector consists of a scintillating crystal, which has a 3.81 cm diameter and 3.81 cm length, and is enclosed by a 0.5 mm thick aluminum shield. The x-ray emissions serve as a fingerprint of the electron kinetic energy and, thus, are the primary focus of our investigation. In our simulations, we used the Lawrence Livermore National Laboratory physics list, which has been proven to work very well at the energies of interest (<1 MeV). 45 Our Geant4 simulation code is based on example B1 provided in the Geant4 software manual.<sup>47</sup> The version and patch of Geant4 used in this investigation were version 4.10.05 and patch-01. A screenshot of the Geant4 graphical user interface, showing the simulation setup, is shown in Fig. 1(c).

Our simulation setup mirrors the experiments performed by da Silva *et al.*, <sup>1</sup> who measured x-ray emissions from  $\sim 100\,\mathrm{kV}$  streamer discharges in an 8 cm rod-to-plane discharge gap. More specifically, it mirrors "case A" in their Table I. These authors constructed spectra of x-ray energies deposited in the detector by collecting x-ray emissions from hundreds of electrical discharges, assumed to be identical. In this

**TABLE I.** Summary of algebraic tools for combining and creating new electron beams and their x-ray energy spectra. The check marks ( $_{\lor}$ ) indicate which type of spectra can be recreated with a given technique.

| Section | Operation                     |           | Number<br>of photons<br>detected | 01        | Application(s)              |
|---------|-------------------------------|-----------|----------------------------------|-----------|-----------------------------|
| II B 1  | Weighted sum of distributions | √         |                                  |           | Interpolation               |
| II B 2  | Convolution                   |           |                                  | $\sqrt{}$ | Interpolation and Synthesis |
| II B 3  | Random<br>sampling            |           |                                  | $\sqrt{}$ | Interpolation and Synthesis |
| II B 4  | Random combination            | $\sqrt{}$ | $\sqrt{}$                        | $\sqrt{}$ | Synthesis                   |

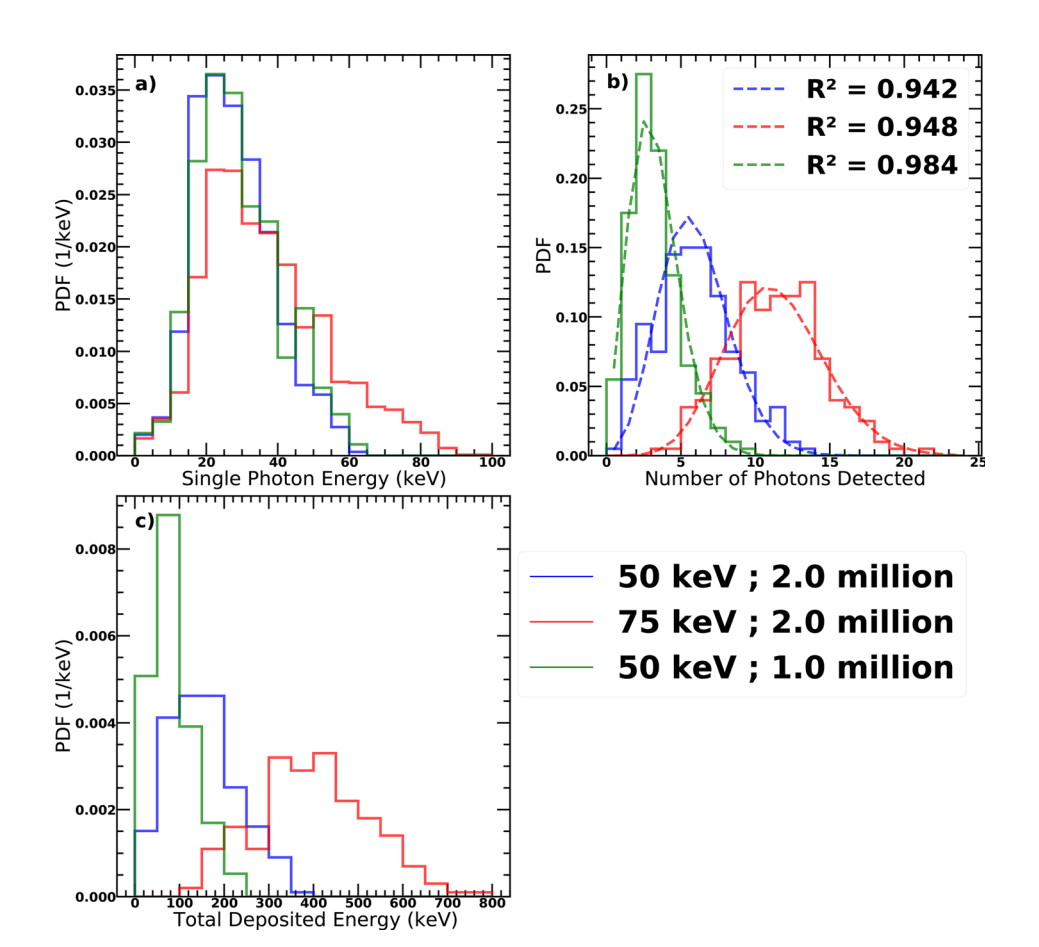


FIG. 2. Three sample monoenergetic electron beam x-ray spectra from: two 50-keV beams, one with  $1 \times 10^6$  and another with  $2 \times 10^6$  electrons, plus one 75-keV beam with  $2 \times 10^6$  electrons. Results for each monoenergetic beam are shown by curves in different colors, as listed in the legend. (a) Single-photon energy spectrum, shown as a probability distribution function (PDF) in units of  $keV^{-1}$ . (b) PDF of the number of photons arriving simultaneously in the detector. Note that the number of photons detected follows a Poisson PDF, as verified by the fits shown in the figure with excellent coefficients of determination, R2. (c) Spectra of x-ray energies deposited in the detector (PDF in units of keV<sup>-1</sup>). This quantity is what is typically reported in experimental investigations. Note: in this article when we refer to the beam kinetic energy we always mean the kinetic energy of individual electrons in the monoenergetic beam.

article, we repeat the strategy computationally. For each monoenergetic electron beam energy and electron count, 200 different simulations are performed, each one of them is seeded by a different random number. The results are then aggregated to produce spectral information, as shown in Fig. 2.

Figure 2 shows probability distributions for: individual photon energies [Fig. 2(a)], number of photons detected [Fig. 2(b)], and total energy deposited in the detector [Fig. 2(c)], for three sample monoenergetic beams. Hereafter, these three distributions are referred to as  $p(\mathscr{E}),\,p(N;\langle N\rangle)$ , and  $p(\mathscr{E}_{\mathrm{dep}})$ , respectively. The beam energies and their corresponding electron counts are listed in the main figure legend. Three key points must be highlighted from this figure. First, the single photon energy spectrum tail gets longer for higher beam energies, but it is independent of the number of electrons in the source beam [Fig. 2(a)]. Also note that the maximum photon energy is higher than the initial beam kinetic energy. This happens because electrons gain more energy from the gap field before producing Bremsstrahlung x-rays. Second, we verify that the amount of photons intercepted by the detector is a Poisson process (similar to the findings of Carlson et al. 48) by fitting a Poisson function over our data. The analytical expression for the Poisson distribution is given by

$$p(N;\langle N\rangle) = \frac{\langle N\rangle^N e^{-\langle N\rangle}}{N!},\tag{1}$$

where N is the number of photons arriving at the detector each time (i.e., the independent variable), and  $\langle N \rangle$  is the average number of photons arriving at the detector (i.e., the parameter that defines the distribution shape). We calculate  $\langle N \rangle$  from the results of the Geant4 simulations, plug into Eq. (1), and compare to the distributions derived directly from the Monte Carlo simulations. The good agreement is evidenced by the high-value of the coefficient of determination  $(R^2)$  listed in the Fig. 2(b) legend. Figure 2(b) shows that multiple photons usually arrive at the same time at the detector (up to 22 for the particular cases shown in the figure), this is what we refer to as photon pileup in this paper. Third, the deposited energies shown in Fig. 2(c) are what really can be measured in a laboratory experiment. It is easy to see that the deposited energy spectra has a complicated dependence on both the number of electrons in the beam and the initial electron kinetic energy, and that in principle it may be very different from the single-photon energy spectrum itself. Figure 2 makes the case that, due to ambiguities arising from photon pileup, it can be very difficult to retrieve the runaway electron properties solely based on the deposited energy spectra.

# B. Algebraic tools for creating and combining electron beams

The ultimate goal of this paper is to reproduce x-ray deposited energy spectra emitted by runaway electrons with an arbitrary energy

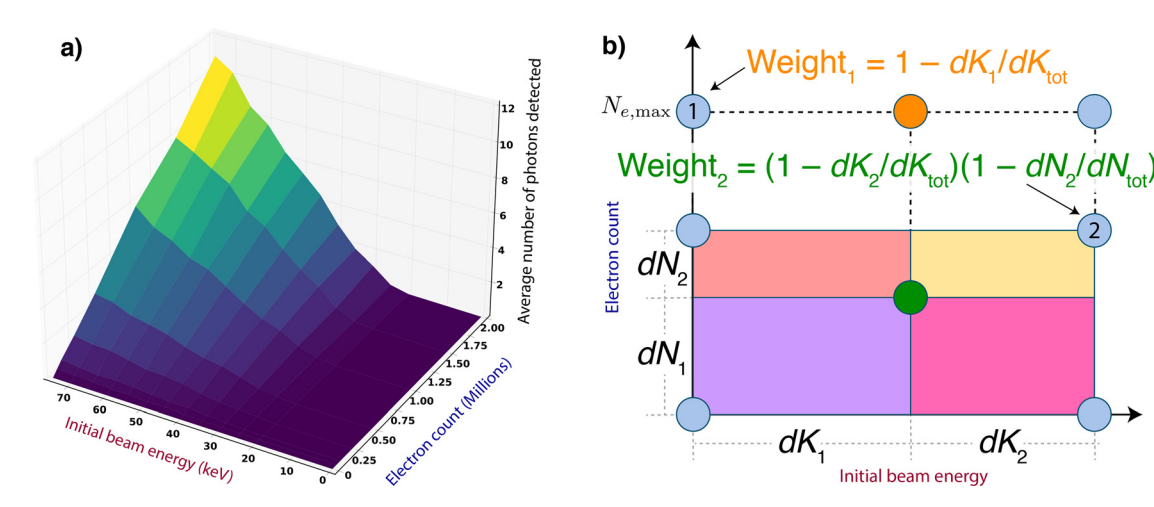


FIG. 3. (a) A three-dimensional plot showing the average number of photons detected (sheet height) as a function of initial electron count and initial beam energy. (b) Schematical representation of the two-dimensional linear interpolation algorithm used. In order to create beams within the grid of pre-tabulated simulations, we use bi-linear interpolation (green dot). For points at the edge of the domain (orange dot), a simple, 1D linear interpolation is used instead.

distribution, such as what is obtained in laboratory measurements (see, for instance, Fig. 4 of da Silva  $et\ al.^1$ ). In this work, we aim to devise a strategy to relate the spectrum of runaway electrons at the source to the x-ray photons collected by the detector. This is done by combining an ensemble of monoenergetic beams, as described below. We start by extending the simulations shown in Fig. 2 to cover the 20 to 75 keV energy range (in steps of 5 keV), and for beams with electron counts ranging between  $5 \times 10^4$  and  $2 \times 10^6$  electrons (in steps of up to  $5 \times 10^5$ ). The resulting grid of simulations is shown in Fig. 3(a). The vertical axis (or the sheet height) shows the average number of photon detections (up to 10). In our approach, these monoenergetic electron beam simulations serve as basis functions, which can be superposed to create general-shape electron energy spectra. The strategies used for creating and combining electron beams are described in detail in Secs. II B 1–II B 4.

# 1. Weighted sum of distributions

Weighted sum of distributions is a method for interpolation devised to create a monoenergetic beam with any energy and number of electrons within the existing grid based on information from the four nearest neighbors, which are results of direct Geant4 simulations. When an initial electron count and beam energy are requested, a unit rectangular area is created around the requested point, with corners at the four nearest catalogued simulations. The area is divided into quadrants, and each of these four subareas is then designated as a weight corresponding to the distribution at the nearest corner. The unit rectangle is schematically shown in Fig. 3(b). Mathematically, the weight associated with each corner is  $(1 - dK_i/dK_{\text{tot}})(1 - dN_i/dN_{\text{tot}})$ , where  $dK_i$  and  $dN_i$  are the distances to the point of interest, and  $dK_{tot}$  $= dK_1 + dK_2$  and  $dN_{\text{tot}} = dN_1 + dN_2$  are the total dimensions of the rectangle, equal to the increment in electron energy or number of electrons that discretizes the "quilt" in Fig. 3(a). Any of the three probability distributions (shown in Fig. 2) for the point of interest is then recreated as a weighted sum of the distributions of the four neighboring points. Additionally, the entire distribution is renormalized to ensure that the area under the probability distribution function (PDF) curve is 1. When recreating a point inside of the domain [green dot in Fig. 3(b)], this algorithm is equivalent to a bilinear interpolation. On the other hand, if the desired point lies at one of the edges of the domain (orange dot in the figure), a simple linear interpolation is sufficient. In this case, the weight is given based on the distance to the point of interest, as  $1-K_i/K_{\rm tot}$ , for a point at one of the  $N_e$  edges of the domain. When reconstructing the single-photon energy distribution,  $p(\mathscr{E})$ , it is convenient to replace the green dot by the orange one altogether (with  $N_e=N_{e,\rm max}=2\times10^6$ ), since  $p(\mathscr{E})$  does not depend on the electron count, and the case with the highest number of photon detections yields the most trustworthy statistics.

The distribution of the number of photons detected is well represented by a closed-form parametric distribution, as shown in Eq. (1) and Fig. 2(b). Thus, when recreating the distribution of photons arriving at the detector, we use the procedure above to interpolate the sheet shown in Fig. 3(a) to recreate  $\langle N \rangle$ , and then we plug it into Eq. (1) to reconstruct the desired distribution.

# 2. Convolution

Convolution is a short-hand name to an alternative method used to reconstruct the distribution of energy deposited in the detector [same as shown in Fig. 2(c)]. Convolution of probability distributions is commonly used to derive the probability distribution of sums of random variables. Mathematically, the distribution of deposited energies is expressed as

$$p(\mathscr{E}_{\text{dep}}) = \sum_{N=1}^{N_{\text{max}}} p(N; \langle N \rangle) C(\mathscr{E}; N), \tag{2}$$

where  $p(N; \langle N \rangle)$  is the probability of N photons arriving at the detector given by Eq. (1), and  $C(\mathcal{E}; N)$  is the resulting photon energy ( $\mathcal{E}$ ) distribution when N photons arrive simultaneously at the detector. For N=1,  $C(\mathcal{E}; N=1)$  is simply the single photon energy distribution  $p(\mathcal{E})$ , such as shown in Fig. 2(a). However for higher N values, this

quantity is recursively defined by the following convolution:  $C(\mathscr{E};N) = p(\mathscr{E}) \otimes C(\mathscr{E};N-1)$ . This is why we refer to this method as "convolution." The method outlined in this subsection is an alternative to the weighted sum of distributions (introduced in Sec. IIB1) for recreating the distribution of deposited energies whenever  $p(N;\langle N\rangle)$  and  $p(\mathscr{E})$  are known.

If both  $p(N; \langle N \rangle)$  and  $p(\mathscr{E})$  are represented by closed-form distributions,  $p(\mathscr{E}_{dep})$  may also be represented in closed form. For instance, if  $p(\mathscr{E})$  is given by an Exponential distribution, the resulting  $p(\mathscr{E}_{dep})$  is given in closed-form by the Erlang distribution, as noted by Carlson *et al.*<sup>48</sup> [see their Eqs. (2), (3), and (4)].

#### 3. Random sampling

Random sampling is another alternative method for generating the spectrum of deposited energies from the known spectra of single-photon energies and number of detected photons. This is done by drawing random numbers from the  $p(N;\langle N\rangle)$  and  $p(\mathscr{E})$  distributions a large number of times and combining this information to construct  $p(\mathscr{E}_{\text{dep}})$ . More precisely, one detection (equivalent to one Geant4 simulation or one spark trigger) is generated by drawing the number of photons arriving at the detector from  $p(N;\langle N\rangle)$ . Let's say that the result is 3. Then three photons are drawn from  $p(\mathscr{E})$  and their total energy is summed up to yield  $\mathscr{E}_{\text{dep}}$ . All  $\mathscr{E}_{\text{dep}}$  values are then histogrammed to construct the compound probability distribution  $p(\mathscr{E}_{\text{dep}})$ .

Algorithmically, one may proceed as follows to obtain the photon energy, for example. First, a random number r is drawn between 0 and 1. Second, the cumulative distribution function,  $\mathrm{CDF}(\mathscr{E}) = \int_0^{\mathscr{E}} p(\mathscr{E}') d\mathscr{E}'$ , is inverted to yield an energy value,  $\mathscr{E} = \mathrm{CDF}^{-1}(r)$ . Thus, likelihood of being selected is related to the weight associated with that energy value in the distribution. Since a very large number of artificial detections can be created with random sampling, this technique works very well in cases where data are scant, e.g., for lower-energy or lower-count beams. This technique is in some ways analogous to the bootstrapping method used in statistics.

#### 4. Random combination

Random combination is used to combine beams together. Here, a new distribution is created by randomly summing the constituent components of the distributions. For example, consider two distributions created from two data sets [A, B, C, D] and [a, b, c, d], where each of the elements may be the single-photon energies, the number of photons detected, or the total photon energy deposited in the detector. In principle, the two sets can be combined by summing the elements of both arrays, i.e., [A+a, B+b, C+c, D+d]. After the summation is performed, the probability distributions of interest can be created. When the two arrays listed above correspond to lists of individual photon energies, the addition operation "+" in A+a corresponds in practice to a concatenation of both arrays.

Combination can be further expanded upon by randomization. Given two or more arrays, entries from every array are selected from a random index and then summed together, yielding for instance, something like [B+c, A+d, C+b, D+a, A+a, C+d, ...]. This method, shorthanded *random combination*, improves upon a simple addition in several ways. First, the random selection of elements allows for arrays of varying lengths to be summed together, so no array needs to be truncated or artificially expanded. Second, a large number of different random combinations can be created, up to  $\prod_i M_i = M_1 \cdot M_2 \cdot M_3...$ , where  $M_i$ 

is the number of entries in the *j*th set. In the example above, consisting of two sets with four entries each, a total of 16 different combinations are possible. The combined data set may effectively have a population size  $(\prod_i M_i)$  much larger than the original ones  $(M_i)$ .

### 5. Summary of algebraic tools

A summary of the algebraic tools is provided in Table I. The table indicates which type of spectra can be reconstructed with each technique, and what are the key application(s) of each of the proposed methods. In the far-right column, *interpolation* refers to the creation of monoenergetic beams within the grid of pre-tabulated simulations [Fig. 3(a)], while *synthesis* refers to the addition of two or more electron beams to create new beams (including ones with more electrons than in the pre-tabulated simulations), or to create spectra of arbitrary shape. As discussed and justified in Sec. III below, the weighted sum of distributions is the preferred technique for beam interpolation, while the random sampling is the preferred technique for creating synthetic  $p(\mathscr{E}_{dep})$  spectra.

#### III. RESULTS

# A. Monoenergetic electron beam properties

Figure 4 shows average properties of the simulated monoenergetic beams as a function of the kinetic energy of electrons in the beam. Each curve in the figure corresponds to beams with an increasing number of electrons  $(N_e)$ . Each data point in the figure is the aggregate result of 200 Geant4 simulations seeded by different random numbers. The four panels in the figure show: the average energy of detected photons [Fig. 4(a)], the average number of photons detected [Fig. 4(b)], the average energy deposited in the detector [Fig. 4(c)], and the detection frequency [Fig. 4(d)]. Error bars are one standard deviation, shown only for the 0.5 and  $2 \times 10^6$  electron cases to avoid cluttering the figures. The average photon energy  $\langle\mathscr{E}\rangle$ does not depend on  $N_e$ , and thus all curves in Fig. 4(a) naturally lie on top of each other. On the other hand, the average number of photons arriving at the detector  $\langle N \rangle$ , and the average x-ray energy deposited in the detector  $\langle \mathscr{E}_{dep} \rangle$ , are directly proportional to  $N_e$ . For this reason, the curves in Figs. 4(b) and 4(c) are normalized to the number of electrons in the monoenergetic beam. Similarly, the displayed error bars are normalized as well.

The data in Figs. 4(a)–4(c) can be approximately fitted by a polynomial expression in the form  $\alpha(K/K_{\rm max})^2+\beta(K/K_{\rm max})+\gamma$ , where K is the initial kinetic energy of electrons in the beam in units of keV,  $K_{\rm max}=75\,{\rm keV}$  is a normalization value, and  $\alpha$ ,  $\beta$ , and  $\gamma$  are the fit constants. The coefficients that best fit the data are listed in Table II. The normalization to  $K_{\rm max}$  ensures that the units of  $\alpha$ ,  $\beta$ , and  $\gamma$  are the same ones as of the quantities on the left-hand side; the units are listed in the table's fourth column. The far-right column shows the average  $R^2$  value when comparing the fit to all four curves shown in each figure. It can be seen from Fig. 4 and Table II that  $\langle\mathscr{E}\rangle$  and  $\langle N\rangle/N_e$  have mostly a linear dependence on the electron energy, as evidenced by the dominance of the  $\beta$  coefficient. In contrast,  $\langle\mathscr{E}_{\rm dep}\rangle/N_e$  mostly trends quadratic with K. The fits for  $\langle N\rangle/N_e$  and  $\langle\mathscr{E}_{\rm dep}\rangle/N_e$  do not perform well for energies lower than  $\sim 30\,{\rm keV}$ .

According to Attix<sup>50</sup> (p. 214), the Bremsstrahlung emission efficiency of a monoenergetic electron beam impingent on a thick target can be approximated as  $\langle \mathscr{E}_{\text{emit}} \rangle / N_e = \kappa Z K^2$ , where  $\langle \mathscr{E}_{\text{emit}} \rangle$  is the expected total x-ray energy emitted, Z is the target (ground electrode) atomic number, and  $\kappa \simeq 10^{-6}\,\text{keV}$  is a constant.<sup>50–52</sup> The emitted x-

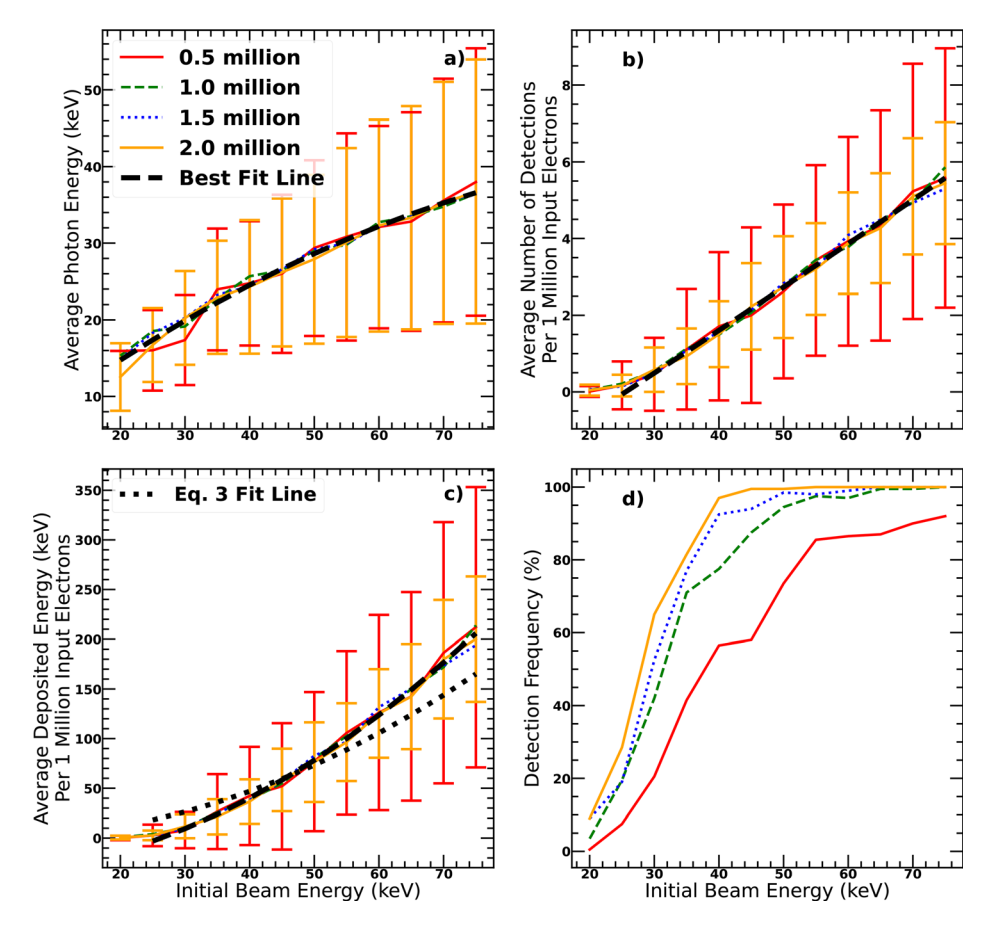


FIG. 4. Properties of monoenergetic beams with initial electron energies from 20 to 75 keV in steps of 5 keV. The four panels are plotted against the initial kinetic energy of electrons in the beam. (a) Average energy of individual photons detected. (b) Average number of detections. (c) Average x-ray energy deposited in the detector. (d) Detection frequency (in %). Error bars represent one standard deviation. Curves in panels (b) and (c) are normalized to the number of electrons in the beam.

ray energy can be converted to deposited (or detected) energy by accounting for two factors: the solid angle (=  $\mathcal{A}_{\text{det}}/4\pi d^2$  for an isotropic source, where  $\mathcal{A}_{\text{det}}$  is the detector surface area and d is the source-detector distance) and attenuation in air (= $e^{-\mu d}$ , where  $\mu = 0.065$  m<sup>-1</sup> is the linear attenuation coefficient of 25-keV x-rays in air, swhich corresponds to a typical x-ray energy in our data set). Combining these effects, we reach the following expression for the expected detected energy:

$$\frac{\langle \mathcal{E}_{\text{dep}} \rangle}{N_e} = \kappa Z \frac{\mathcal{A}_{\text{det}}}{4\pi d^2} e^{-\mu d} K^2. \tag{3}$$

This equation has the same shape as the fits shown in Table II, but with  $\beta=\gamma=0$ . The resulting  $\alpha$  coefficient is shown in the table. The simple formula (3) derived and discussed in this paragraph performs

well against the direct results of Monte Carlo simulations (see the  $R^2$  value in the right-most column). If nothing else, it helps illustrate the origin of the quadratic dependence of  $\langle \mathscr{E}_{\text{dep}} \rangle$  on K, displayed in Fig. 4(c).

The detection frequency, shown in Fig. 4(d), simply represents the % fraction of all simulations in which at least one photon has been detected. As a point of comparison, in case A of da Silva's experimental data<sup>1</sup> (which directly maps to the simulation setup used here), photons were detected in about 60% of all discharge triggers.

# **B. Beam interpolation**

Three different methods can be used to create beams within the pre-existing grid of simulations, i.e., to perform beam interpolation. The primary one is the weighted sum of distributions described in Sec. II B 1.

**TABLE II.** Curves in Figs. 4(a)-4(c) can be well fit by a polynomial expression in the format  $\alpha(K/K_{max})^2 + \beta(K/K_{max}) + \gamma$ , with fit coefficients  $\alpha$ ,  $\beta$ , and  $\gamma$  as given in the table.

| Quantity averaged          | Figure | Expression   | Units                   | α      | β     | γ      | $R^2$ |
|----------------------------|--------|--|-------------------------|--------|-------|--------|-------|
| Single-photon energy       | 4(a)   | $\langle \mathscr{E}  angle$                       | keV                     | -14.7  | 48.4  | 2.89   | 0.987 |
| Number of detected photons | 4(b)   | $\langle N \rangle/N_e$                            | $10^{-6}$               | 0.25   | 8.13  | -2.8   | 0.985 |
| Deposited x-ray energy     | 4(c)   | $\langle \mathscr{E}_{\mathrm{dep}} \rangle / N_e$ | $10^{-6}  \mathrm{keV}$ | 209.3  | 34.27 | -37.76 | 0.992 |
| Dep. x-ray energy, Eq. (3) | 4(c)   | $\langle {\mathscr E}_{ m dep}  angle / N_e$       | $10^{-6}\mathrm{keV}$   | 163.71 | 0     | 0      | 0.907 |

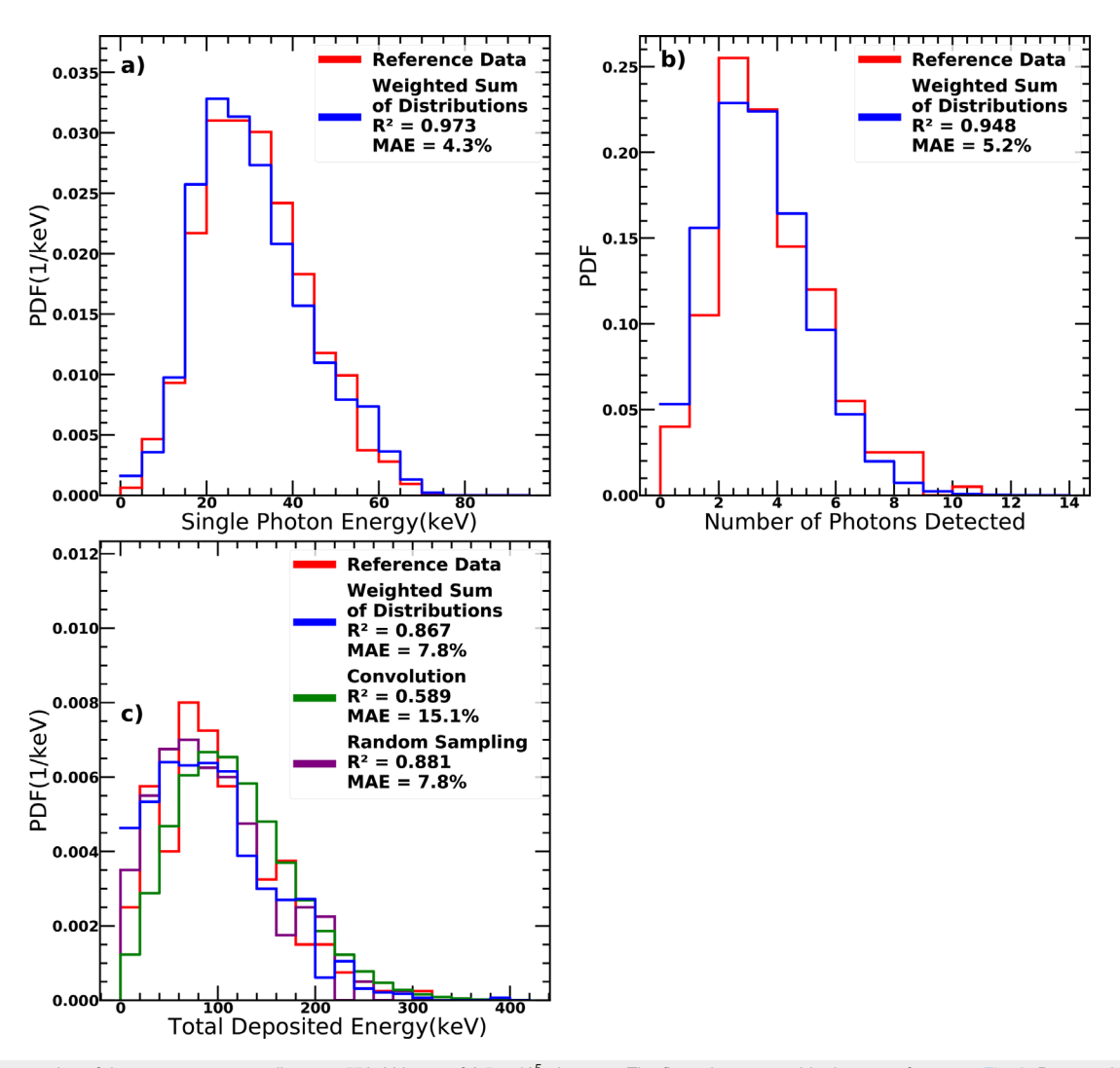


FIG. 5. Reconstruction of the spectra corresponding to a 57 keV beam of  $8.5 \times 10^5$  electrons. The figure is presented in the same format as Fig. 2. Presented in red is the direct Geant4 data of such a run. Presented in blue is the interpolation by method of weighted sum of distributions. (a) Single-photon energy spectrum. (b) Distribution of number of photons arriving at the detector. (c) Spectrum of deposited energies. Panel (c) shows how the convolution (green curve) and random sampling (purple) compare to the weighted sum of distributions.

This method can reconstruct all three types of spectra of interest:  $p(\mathscr{E}), p(N; \langle N \rangle)$ , and  $p(\mathscr{E}_{dep})$ . Additionally, there are two alternative methods for reconstructing the spectrum of energies deposited in the detector: the method of convolution described in Sec. II B 2, and the method of random sampling described in Sec. II B 3. In order to validate our beam interpolation algorithms, we ran a test run of 57 keV and  $8.5 \times 10^5$  electrons, a combination not available in our catalogued Geant4 runs. The comparison is shown in Fig. 5. The accuracy of all methods is evaluated using the R-squared value  $(R^2)$ , as well as the mean average error (MAE in %), between the reconstructed  $p_{rec}$  and reference  $p_{ref}$  distribution. The MAE is normalized to the peak value of the reference distribution as MAE =  $\langle | p_{rec} - p_{ref} | / \max(p_{ref}) \rangle$ .

As can be seen in Fig. 5, the weighted sum of distributions is excellent at reproducing the three types of spectra. The two alternative methods for recreating  $p(\mathcal{E}_{dep})$  perform reasonably well, but not as

well the weighted sum of distributions. For quantitative assurance, the reader is referred to the  $R^2$  and MAE values in the legend of Fig. 5(c).

#### C. Monoenergetic beam synthesis

Synthesis is the process of combining multiple beams to produce electron energy spectra of any desired shape. In order to ensure that our methods are accurate, we start by synthesizing the simplest type of spectrum—a monoenergetic beam. Here, we combine two 50 keV beams, with  $1\times10^6$  electrons each, into a single 50 keV beam with  $2\times10^6$  electrons. The results of our beam synthesis procedure is then compared to an independent 50 keV beam,  $2\times10^6$  electrons Geant4 simulation, as shown in Fig. 6.

Figure 6 shows that the primary synthesis technique, random combination, performs very well in reproducing the three types of spectra of interest. The mean average error in reconstructing the

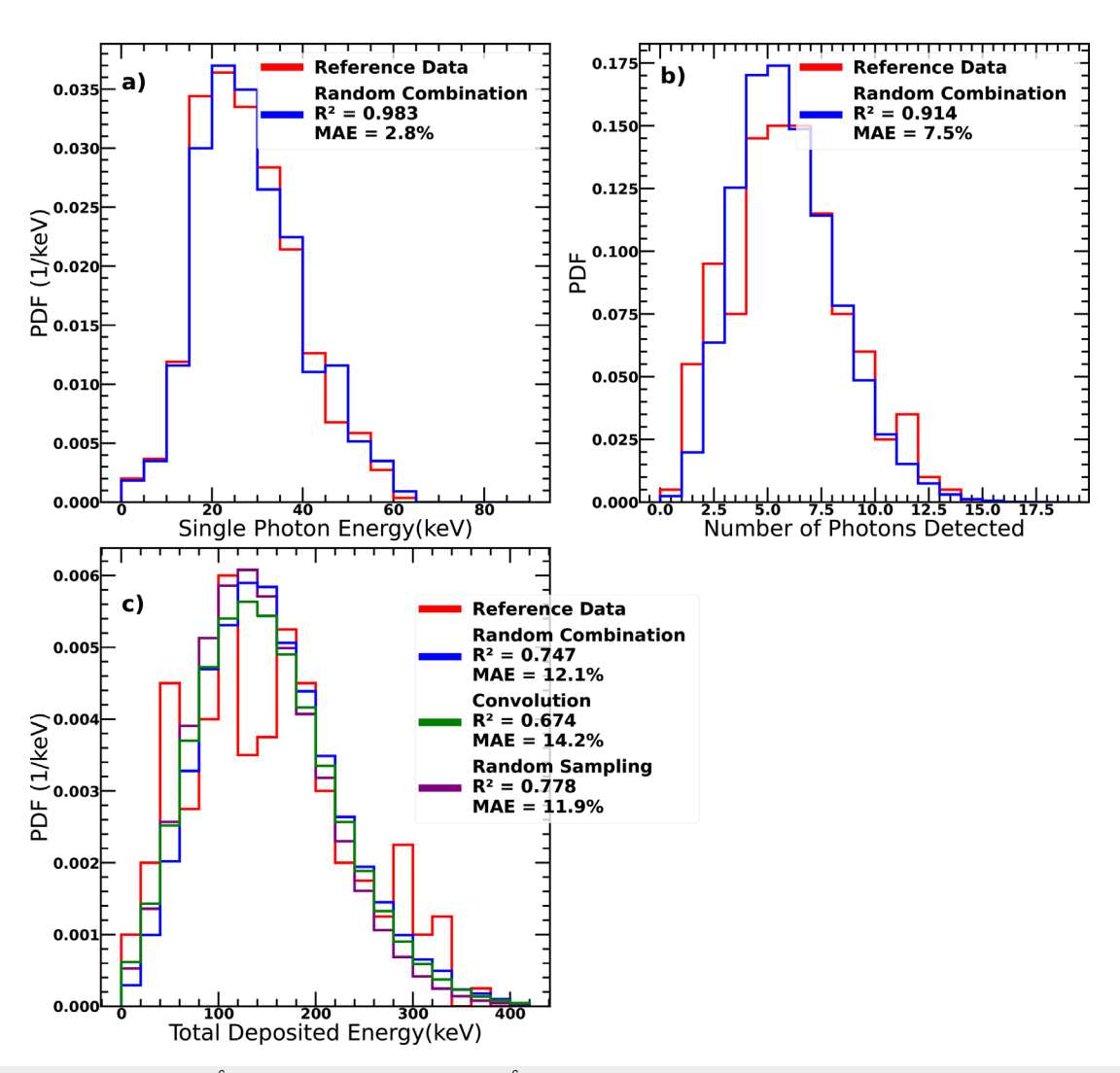


**FIG. 6.** Reconstruction of a 50 keV,  $2 \times 10^6$  electron beam from two 50 keV,  $1 \times 10^6$  electron beams. The figure is presented in the same format as Fig. 2. The red curves correspond to the direct Geant4 run of a 50 keV,  $2 \times 10^6$  electron beam run. Presented in blue is the synthesis via random combination. (a) Single-photon energy spectrum. (b) Distribution of number of photons arriving at the detector. (c) Spectrum of deposited energies. Panel (c) shows how the convolution (green curve) and random sampling (purple) techniques compare to random combination.

single-photon energy, the number of detections, and deposited energy spectra is 2.8, 7.5, and 12.1%, respectively. The alternative methods for reconstructing  $p(\mathscr{E}_{\text{dep}})$  also perform well. Interestingly, the random sampling technique further improves the reconstruction and yields higher  $R^2$  and lower MAE values. Additionally, we have noticed that the randomization aspect of the random combination technique does not improve the reconstruction of the single-photon energy spectrum. In other words, simply concatenating the photons in the two beams and histogramming them into  $p(\mathscr{E})$  yields a satisfactory result.

# D. Synthesis of general-shape spectra

In this section, we discuss how monoenergetic electron beams can be combined to create electron energy spectra of general/arbitrary shape, and proceed to discuss how photon pileup ambiguities manifest themselves. The general question we are posing is what is the electron energy distribution  $N_e=N_e(K)$  that can best reproduce the experimental data collected in the laboratory. Note that  $N_e$  is not a normalized probability distribution function. The results are shown in Fig. 7 and described below. The blue curve in Fig. 7(b) shows the spectrum of deposited energies corresponding to case A in the experimental data, which best matches the Geant4 simulation setup used here. This distribution is constructed by repeating the experiment  $\sim$ 600 times and histogramming the detected x-ray energy. The spectrum shown in Fig. 7(b) has two peaks, with the second one at about 320 keV due to detector pulse height saturation. The maximum expected energy of single photons is 100 keV, because that is also the maximum expected kinetic energy gained by electrons under the 100 kV gap voltage. It is easy to see that the  $p(\mathscr{E}_{\text{dep}})$  distribution extends well beyond that and even beyond the saturation level of the detector. As discussed earlier,

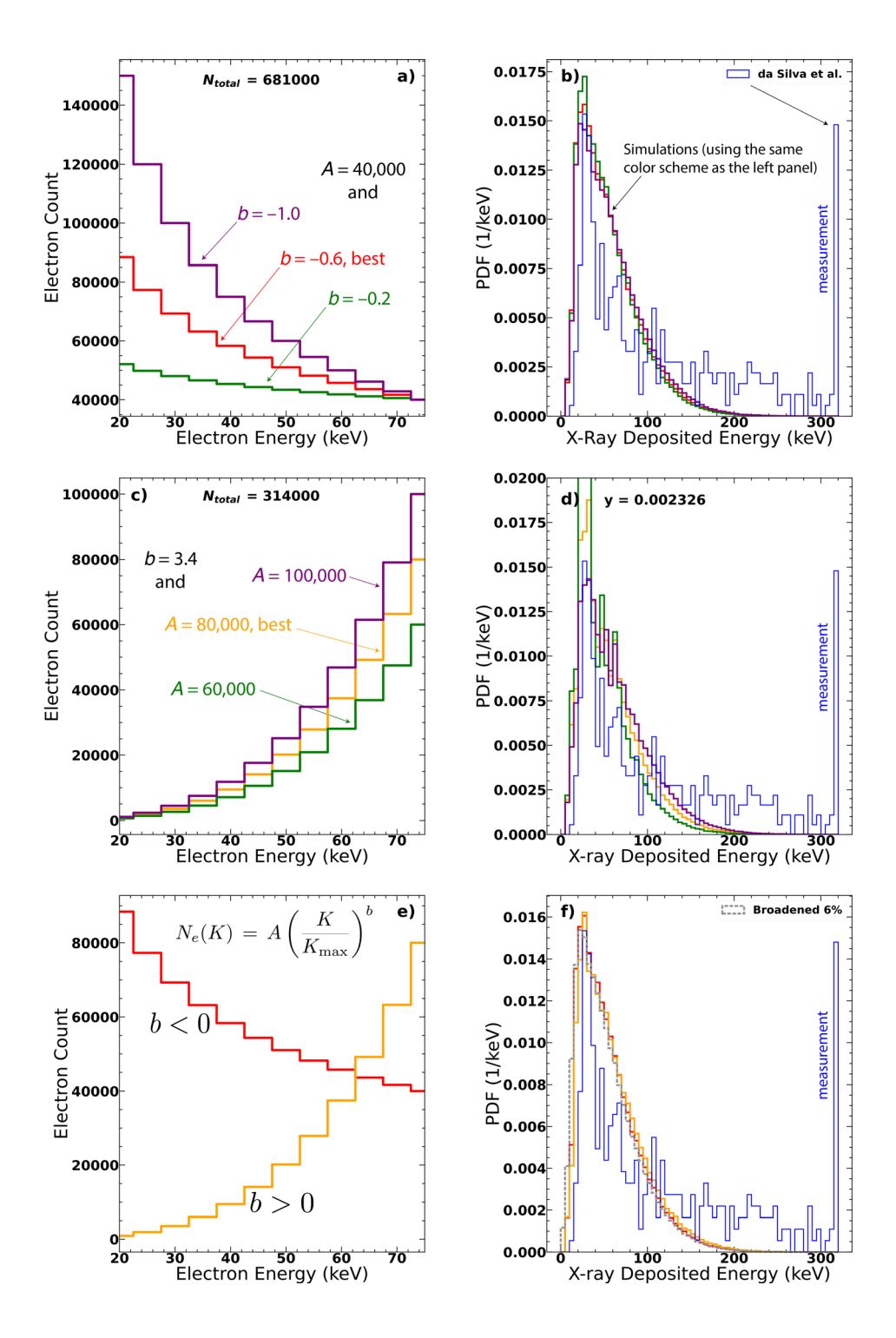


FIG. 7. Power-law electron energy spectra at the source (left), resulting x-ray deposited energy spectra (right), and comparison to measurements (blue curves on right-hand side panels). Fit coefficients and associated errors are listed in Table III. (a) and (b) Attempt to fit the deposited energy curve using a decreasing power law. (c) and (d) Attempt to fit the deposited energy curve using an increasing power law. (e) and (f) Comparison between the optimal cases for the increasing and decreasing power laws. The  $N_{\rm total}$  presented in panels (a) and (c) are the total number of electrons in the beam for the optimal case in that panel. Panel (f) also shows the effects of Gaussian broadening due to limited energy resolution in the detector. A 6% Gaussian broadening is applied to the red curve, and the resulting effects are shown as a gray dashed curved in the same figure.

this happens due to photon pileup, i.e., due to the fact that every time a successful detection is made, multiple photons arrive at the detector virtually at the same time.

In order to constrain the number of free parameters we are operating with, we use a simple two-parameter, monotonic function to

describe the electron energy spectrum. We assume that the electron distribution follows an inverse power law  $N_e(K) = A(K/K_{\text{max}})^b$ , with b < 0. For a given choice of A and b parameters, the synthetic spectra are constructed by first, determining the number of electrons in each beam according to the formula  $N_e(K) = A(K/K_{\text{max}})^b$ , where K takes

**TABLE III.** Coefficients and errors associated with different power law fits for Figs. 7 and 8. The five components of the cost function are:  $1 - R^2$ , the mean average error (MAE), the error at the two peaks (PE1 and PE2), and the detection frequency error compared to the detection frequency reported in case A of the measurements paper (DFE). The weights in the cost function that produced the fits for Fig. 7 were: 0.5, 1, 1, 0.2, and 0.5, for the five terms in the order shown in the table. For obtaining the fits shown in Fig. 8, we swapped the weights of PE1 and PE2.

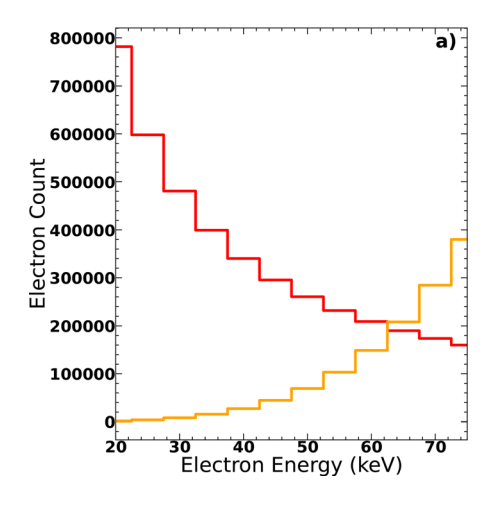
| Figures   | Color   | A       | b    | $R^2$    | MAE (%) | PE1 (%) | PE2 (%) | DFE (%) | Cost (%) |  |  |
|---|---|---------|------|----------|---------|---------|---------|---------|----------|--|--|
|   | Attempts to fit the first peak of the measured x-ray deposited energy distribution (Fig. 7) |         |      |          |         |         |         |         |          |  |  |
| 7(a) and 7(b)   | Red   | 40 000  | -0.6 | 0.4867   | 14.64   | 4.616   | 100     | 26.33   | 24.39    |  |  |
| 7(a) and 7(b)   | Green   | 40 000  | -0.2 | 0.5042   | 14.90   | 17.67   | 100.0   | 19.66   | 27.25    |  |  |
| 7(a) and 7(b)   | Purple  | 40 000  | -1.0 | 0.4814   | 14.11   | 2.94    | 99.96   | 34.30   | 25.03    |  |  |
| 7(c) and 7(d)   | Orange  | 80 000  | 3.4  | 0.4986   | 14.03   | 2.915   | 99.95   | 21.56   | 22.74    |  |  |
| 7(c) and 7(d)   | Green   | 60 000  | 3.4  | 0.5208   | 15.41   | 21.49   | 100.0   | 5.273   | 26.09    |  |  |
| 7(c) and 7(d)   | Purple  | 100 000 | 3.4  | 0.4783   | 12.96   | 15.69   | 99.96   | 33.99   | 28.64    |  |  |
| Attempts to fit the second (saturation) peak of the measured x-ray deposited energy distribution (Fig. 8) |   |         |      |          |         |         |         |         |          |  |  |
| 8(a) and 8(b)   | Red   | 160 000 | -1.2 | 0.002 25 | 17.78   | 97.03   | 4.667   | 67.62   | 62.30    |  |  |
| 8(a) and 8(b)   | Orange  | 380 000 | 4.2  | 0.01276  | 16.66   | 95.36   | 3.631   | 67.17   | 61.13    |  |  |

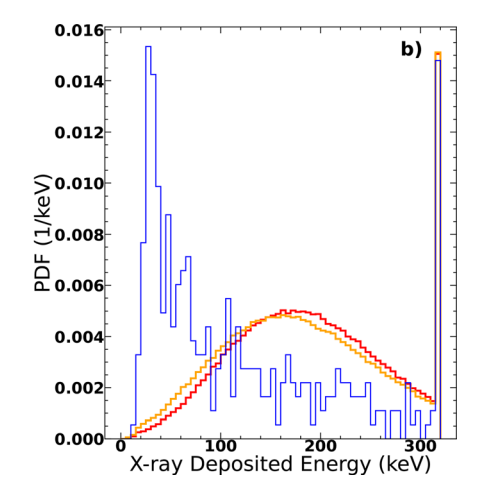
the values 20, 25, 30, ..., 75 keV. If the number of electrons does not coincide with one of the pre-tabulated simulations, the weighted sum of distributions method (Secs. II B 1 and III B) is used to interpolate and provide all beams with the desired  $N_e(K)$  values. Second, after all 12 beams are constructed, their combined x-ray emission spectra are synthesized with the random sampling technique (Secs. II B 3 and IIIC) augmented by random combination. Second, we iteratively adjust the two free parameters (A and b) until the discrepancy between model and measurements reaches a minimum. More precisely, we minimize a cost function given by the following expression: Cost  $=\sum_{i} w_{i} \varepsilon_{i}/W$ . In this summation,  $\varepsilon_{i}$  are five different types of error metrics: the MAE, the error in both peaks (PE1 and PE2), the fraction of variance unexplained by the model (=  $1 - R^2$ ), and the error in detection frequency (DFE). Additionally,  $w_i$  are empirically adjusted weights to ensure that all five error metrics have the desired relative weights to one another, and  $W = \sum_{j} w_{j}$ . All terms in the cost function are given in %.

Our fitting process covered an initial range in A values from 0 to  $2 \times 10^6$  electrons and a range in the exponent b from -8 to 0. The resulting best fit is shown in the top row of Fig. 7 (as the red curve).

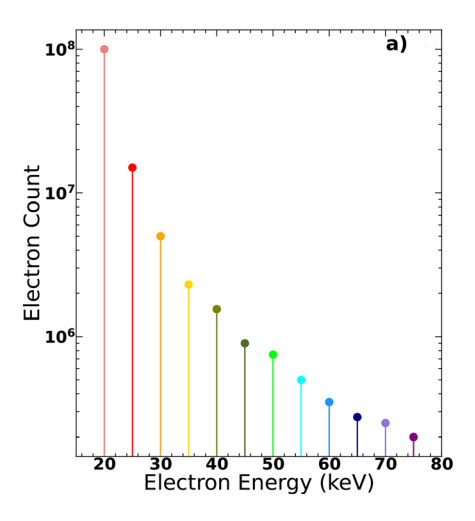
Figure 7(a) shows the inferred electron distribution (red curve), while Fig. 7(b) the resulting  $p(\mathscr{E}_{\text{dep}})$  and comparison with the experimental measurements. The inferred values for A and b that best fit the data are listed in Table III. It can be seen that the inverse power law electron spectrum does a fairly decent job of capturing the low-energy peak in the photon deposited energy spectrum. Figures 7(a)-7(b) also include two other curves with higher and lower power-law indexes b, with values as listed in Table III. The additional curves show that increasing the electron content at low energies (with everything else kept constant) has the role of shifting the primary peak of  $p(\mathscr{E}_{\text{dep}})$  to the right, toward higher  $\mathscr{E}_{\text{dep}}$  values.

It is evident from Fig. 7(b) that an inverse power-law electron energy spectrum cannot simultaneously capture the first peak in  $p(\mathscr{E}_{\text{dep}})$  and its long distribution tail. This may, in principle, be attributed to the fact that runaway electron acceleration is a nonequilibrium process. In such a type of nonequilibrium process, it may be that the system has a large number of electrons in the highest energy levels available. For this reason, we proceed to attempt to fit a spectrum with a monotonically increasing power-law dependence, i.e., with b>0, initially ranging from 0 to 8. The results are shown in the middle row of





**FIG. 8.** Attempts to fit the saturation peak of the measured spectrum of x-ray deposited energies. (a) Power-law electron energy spectra, and (b) resulting  $p(\mathcal{E}_{dep})$ . The fit coefficients and associated errors are listed in the bottom two rows of Table III.



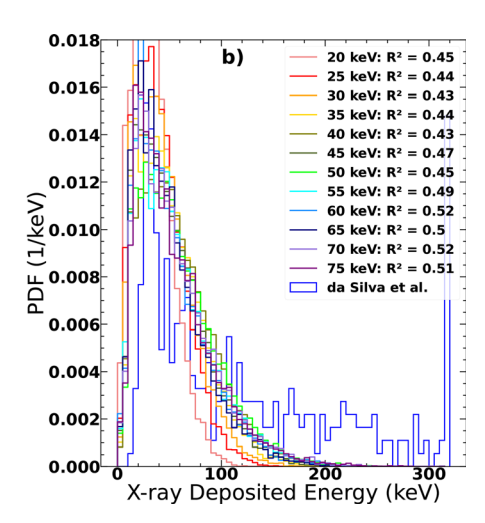
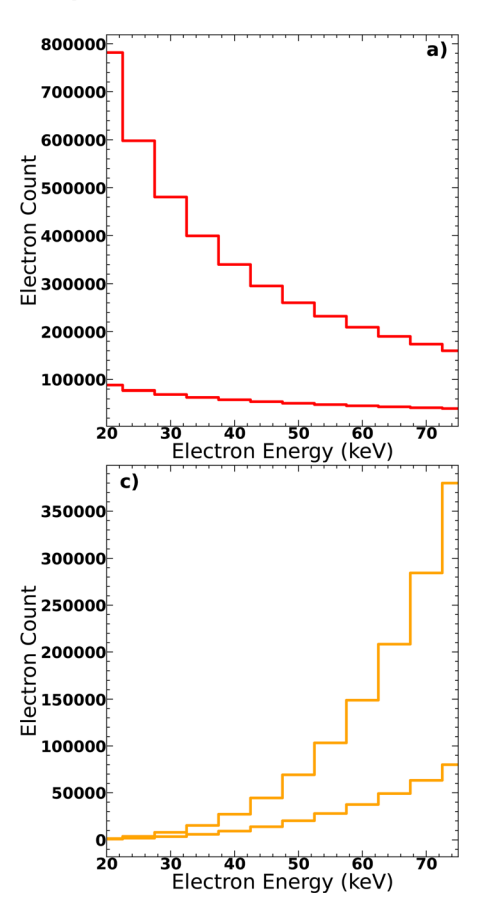


**FIG. 9.** (a) Twelve monoenergetic electron beams. In each one of them the electron count is adjusted so that the resulting  $p(\mathscr{E}_{\text{dep}})$  best matches the measurements (b). For this exercise, the weight of all terms in the cost function with the exception of  $R^2$  are set to zero.

Fig. 7, where the best fit corresponds to the light-orange curve. Figure 7(c) shows the inferred electron distribution, while Fig. 7(d) the resulting  $p(\mathscr{E}_{\text{dep}})$  and comparison with the experimental measurements. The values for A and b that best fit the data are listed in the fourth row of Table III. Remarkably, using the same type of cost function in the optimization problem (i.e., with the same weights  $w_j$ ), yields a best-fit  $p(\mathscr{E}_{\text{dep}})$  spectrum that is nearly identical to the descending power-law

case. The additional curves in Figs. 7(c) and 7(d) show that increasing the electron content at high energies also shifts  $p(\mathscr{E}_{dep})$  toward higher  $\mathscr{E}_{dep}$  values. Nonetheless, this effect is more aggressive in the middle rather than in the top row of Fig. 7.

The bottom row of Fig. 7 emphasizes that the rather different electron energy spectra [Fig. 7(e)] produce nearly identical spectra of photon deposited energies [Fig. 7(f)]. Figures 7(e) and 7(f) illustrate



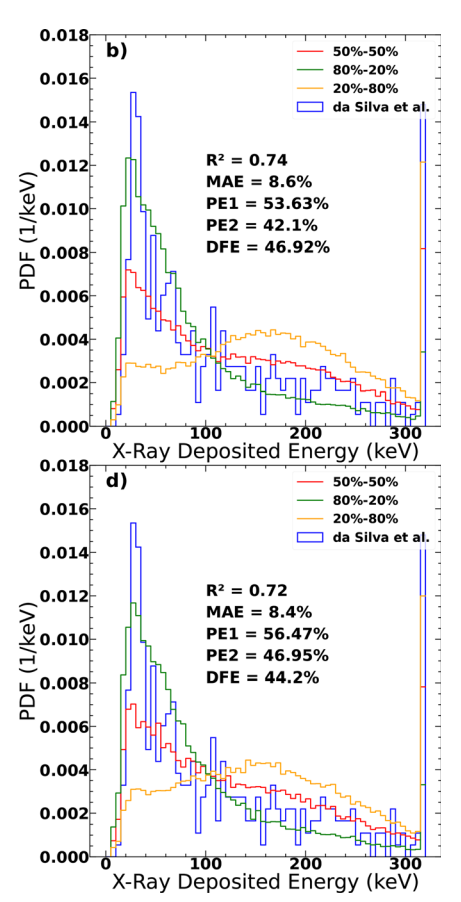


FIG. 10. Power-law electron energy spectra at the source (left), resulting x-ray deposited energy spectra (right), and comparison to measurements (blue curves on right-hand side panels). To create each deposited x-ray energy spectrum, the results of the two electron configurations in the left panels were combined (with relative weights shown). The statistics displayed are for the best case (which is the 50%-50% case). The weights are in order of peak priority, meaning an 80%-20% weight corresponds to a higher contribution from the electron distribution which best fits the first peak. Only the error metrics for the red curves are shown in the right column panels. The top row and bottom rows show results for decreasing and increasing power-law electron energy spectra, respectively.

that the attempt to infer  $p(\mathscr{E}_{dep})$  in a system with photon pileup is an ill-posed problem. This happens even though the level of pileup is not severe. The best fit cases shown in Fig. 7 have an average number of photons detected in a given simulation equal to 1.4 and 1.3, for the ascending and descending power-law spectra, respectively. The inherent ambiguities arise from the fact that increasing the electron content at any portion of the electron spectrum has the same effect of shifting  $p(\mathscr{E}_{dep})$  to the right. This ambiguity can only be alleviated by feeding the automated fitting algorithm progressively more information about the experimental data, such as  $p(\mathscr{E}_{dep})$  collected with the x-ray detector located at several different distances from the source, or with different x-ray filters placed in front of the detector. Such a type of data has been collected previously, and attempting to simulate it will be the subject of subsequent investigations by our team. The total number of electrons for the two best-case fits are listed in Fig. 7. It can be seen that  $3-7 \times 10^5$  electrons are required to explain the measurements, which agrees with the rough estimates provided before.1

Figure 8 shows additional attempts to match the experimentally measured  $p(\mathcal{E}_{\text{dep}})$  with power-law electron energy spectra. However now, the weight associated with the second peak (saturation peak) in  $p(\mathcal{E}_{\text{dep}})$  in the optimization cost function is increased from 0.2 to 1.0, while at the same time the weight associated with the first peak error is reduced from 1.0 to 0.2. The figure shows that the saturation peak can be matched very well, but at the expense of the first one. Generally speaking, more electrons increase the detection frequency. All cases listed in Table III overestimate the experimentally measured detection frequency (see the second-to-last column in the table), which is 59.6%. This detection frequency value implies that 40% of the triggers lie in the  $\mathcal{E}_{\text{dep}} < 5$  keV bin. Please note that this is omitted from the spectra shown in Figs. 7 and 8, to aid the visualization.

# IV. DISCUSSION

Figure 9 is produced to illustrate the origins of the pileup ambiguity. Figure 9 shows 12 different monoenergetic beams between 20 and 75 keV. In each one of them the electron count  $(N_e)$  is adjusted so that the photon deposited energy spectrum best fits the measurements. It can be seen that all 12 beams produce a qualitatively similar  $p(\mathcal{E}_{dep})$ response, and it is not trivial to tell them apart. Increasing the electron count in each beam simply shifts the  $p(\mathscr{E}_{dep})$  peak to the right, and also widens it. This effect can be seen in Fig. 2(c). Figure 9 emphasizes two points: (first) adjusting the electron content at any location (K value) has the same effect, and (second) composite spectra are dominated by the higher-energy beams. Note that one needs 10<sup>8</sup> electrons in the 20-keV beam to produce the same effect as  $2 \times 10^5$  electrons in the 75-keV one. Looking back at the spectra in Figs. 7 and 8, we have revisited it and verified that most of its features can be reproduced by including only beams with  $K \ge 50$  keV. Photon pileup happens for all 12 beams shown in Fig. 9, with the average number of photons intercepted by the detector per simulation ranging between 1.1 and 4.5, for the 75 and 20 keV beams, respectively.

Another source of uncertainty is the variability from one electrical discharge to the next. da Silva *et al.*<sup>1</sup> provided spectra of deposited x-ray energies under the assumption that all electrical discharges are identical. However, due to the stochasticity of electrical breakdown, the actual voltage at which the discharges fire may differ from one discharge to the next. Suppose for instance that the electrical discharges fall into two groups, one that fires at maximum voltage, and produces

higher  $\mathscr{E}_{\text{dep}}$  on average, as shown in Fig. 8, and another that misfires (i.e., fires earlier than expected at a lower applied voltage), and produces lower average  $\mathscr{E}_{\text{dep}}$ , such as shown in Fig. 7. In Fig. 10 we entertain this possibility and reconstruct  $p(\mathscr{E}_{\text{dep}})$  [Fig. 10(b)] by drawing  $\mathscr{E}_{\text{dep}}$  50% of the time from each of the best descending power law fits [Fig. 10(a)], the ones that best fit the main (Fig. 7) and saturation (Fig. 8) peaks, respectively. It can be seen that the generated  $p(\mathscr{E}_{\text{dep}})$  [red curve in Fig. 10(b) with error metrics listed in the figure itself] improves substantially upon the "identical discharge" hypothesis, with higher  $R^2$  and lower MAE values than the ones listed in Table III.

Figure 10(b) also shows what happens if the "misfires" happen more often (80%-20% case, green curve) or less often (20%-80% case, yellow curve). The figure illustrates that this effect may be a major source of uncertainty, since the three displayed cases, with different proportions between full-voltage triggers and misfires, generate substantially different  $p(\mathscr{E}_{dep})$ . Additionally, this effect may also explain the long tail in the measured  $p(\mathscr{E}_{dep})$ . Under this hypothesis, the low-energy peak would be (mostly) generated by the misfires (lowervoltage discharges), while the long tail and the saturation peak would arise from higher-voltage discharges. Figures 10(c)-10(d) illustrate the same effect for the best ascending power-law fits. An improvement with respect to the identical discharge hypothesis is also seen in this case. However, it is still not possible to tell apart the descending and ascending power-law electron energy spectra from their x-ray emissions. Figure 10 helps emphasize that this effect needs to be carefully accounted for in future experimental and modeling works.

Finally, we also explore whether effects of instrumental response can help explain the long tail in the measured  $p(\mathscr{E}_{dep})$ . The energy resolution of the LaBr<sub>3</sub>:Ce detector used in the experiment is 6% at 122 keV. We reconstruct  $p(\mathscr{E}_{dep})$  for the best descending power-law electron energy spectra shown in Fig. 7(e) with added 6% Gaussian broadening to mimic the effects of the detector's energy resolution. This is done by generating a Gaussian distribution centered at  $\mathscr{E}_{dep}$  and with a width of 1.06  $\mathscr{E}_{dep}$ , for each  $\mathscr{E}_{dep}$  value, and then redrawing  $\mathscr{E}_{dep}$  from it. The resulting broadened  $p(\mathscr{E}_{dep})$  spectrum is shown as a gray dashed curve in Fig. 7(f). The difference with respect to the red curve is insignificant and cannot explain the long tail in the measurements (blue curve in the same figure).

# V. CONCLUSIONS

In this work, we presented Geant4 simulations of runaway electrons produced by short laboratory discharges. In the simulations, we represent the runaway electrons by a series of monoenergetic electron beams injected in the spark gap. The initial energy of electrons varies between 20 and 75 keV, but electrons are allowed to accelerate and gain additional energy from the average gap field, of 12.5 kV/cm. The runaway electrons produce Bremsstrahlung x-ray emissions when they hit the ground electrode. After characterizing the x-ray emissions from the monoenergetic beams, we devised a series of algebraic operations that allow us to combine and create new beams from an existing grid of simulations. A substantial amount of work has been done in this paper to validate the proposed methods. Aided of these tools, we proceeded to construct electron energy spectra of general shape, their resulting x-ray emissions, and to compare them to laboratory measurements. The strategies devised can, to some extent, reproduce the spectrum of deposited x-ray energies collected in a laboratory experiment. The results indicate that about  $3-7 \times 10^5$  runaway electrons

have been produced in these 8-cm-long, -100 kV discharges. Due to even a moderate amount of photon pileup, the precise shape of the electron energy spectrum cannot be determined and, thus, this methodology can only be employed to determine what are the best fit parameters within a chosen model (determined by other means, such as from first-principles calculations). We show that pileup ambiguities arise from the fact that every single monoenergetic electron beam (simulated) produces photon deposited energy spectra of similar qualitative shape and that increasing the electron count in any beam has the same qualitative effect of shifting the peak of the deposited energy spectrum toward higher energies. Photon pileup ambiguities can be alleviated by feeding the fitting algorithm with progressively more information about the single-photon energy spectrum. These may be done by simultaneously fitting multiple data sets collected with distinct detection configurations, such as different distances and angles, but we leave this exercise for a subsequent investigation. Finally, we have also discussed how an uncertainty in determining the precise voltage at which the discharges happen may translate into a wide range of x-ray burst energies measured. The discharge voltage uncertainty may be the root cause of the long tail in the measured energy spectra, which could not be explained by other means in this investigation.

#### ACKNOWLEDGMENTS

This project was supported by NSF Grant No. AGS-1917069 to New Mexico Tech and by two New Mexico Space Grant Consortium Undergraduate Research Scholarships.

# **AUTHOR DECLARATIONS**

# Conflict of Interest

The authors have no conflicts to disclose.

#### **DATA AVAILABILITY**

The data that support the findings of this study are available from the corresponding author upon reasonable request.

#### **REFERENCES**

- <sup>1</sup>C. L. da Silva, R. M. Millan, D. G. McGaw, C. T. Yu, A. S. Putter, J. LaBelle, and J. Dwyer, "Laboratory measurements of x-ray emissions from centimeter-long streamer corona discharges," Geophys. Res. Lett. 44, 11,174–11,183, https://doi.org/10.1002/2017GL075262 (2017).
- <sup>2</sup>V. F. Tarasenko and S. I. Yakovlenko, "The electron runaway mechanism in dense gases and the production of high-power subnanosecond electron beams," Phys. Usp. 47, 887–905 (2004).
- <sup>3</sup>P. Tardiveau, N. Moreau, S. Bentaleb, C. Postel, and S. Pasquiers, "Diffuse mode and diffuse-to-filamentary transition in a high pressure nanosecond scale corona discharge under high voltage," J. Phys. D **42**, 175202 (2009).
- <sup>4</sup>T. Shao, C. Zhang, Z. Niu, P. Yan, V. F. Tarasenko, E. K. Baksht, A. G. Burahenko, and Y. V. Shutko, "Diffuse discharge, runaway electron, and x-ray in atmospheric pressure air in an inhomogeneous electrical field in repetitive pulsed modes," Appl. Phys. Lett. **98**, 021503 (2011).
- <sup>5</sup>j. R. Dwyer, "Relativistic breakdown in planetary atmospheres," Phys. Plasmas 14, 042901 (2007).
- <sup>6</sup>J. R. Dwyer and M. A. Uman, "The physics of lightning," Phys. Rep. **534**, 147-241 (2014).
- <sup>7</sup>U. S. I. B. E. Carlson and N. G. Lehtinen, "Runaway relativistic electron avalanche seeding in the Earth's atmosphere," Geophys. Res. 113, A10307 (2008).
- <sup>8</sup>C. T. R. Wilson, "The acceleration of  $\beta$ -particles in strong electric fields such as those of thunderclouds," Proc. Cambridge Philos. Soc. **22**, 534–538 (1925).

- <sup>9</sup>G. D. Moss, V. P. Pasko, N. Y. Liu, and G. Veronis, "Monte Carlo model for analysis of thermal runaway electrons in streamer tips in transient luminous events and streamer zones of lightning leaders," J. Geophys. Res. 111, A02307, https://doi.org/10.1029/2005JA011350 (2006).
- <sup>10</sup> A. V. Gurevich, "On the theory of runaway electrons," Sov. Phys. JETP 12(5), 1961 (1961).
- <sup>11</sup>See M. J. Berger, J. S. Coursey, M. A. Zucker, and J. Chang, http://physics.nist.gov/Star for "ESTAR, PSTAR, and ASTAR: Computer programs for calculating stopping-power and range tables for electrons, protons, and helium ions (version 2.0.1)," [National Institute of Standards and Technology (NIST), Gaithersburg, MD, 2005], accessed 8 July 2018.
- <sup>12</sup> A. V. Gurevich, G. M. Milikh, and R. Roussel-Dupré, "Runaway electron mechanism of air breakdown and preconditioning during a thunderstorm," Phys. Lett. A 165, 463–468 (1992).
- <sup>13</sup>J. R. Dwyer, "A fundamental limit on electric fields in air," Geophys. Res. Lett. 30, 2055, https://doi.org/10.1029/2003GL017781 (2003).
- <sup>14</sup>O. Chanrion, Z. Bonaventura, D. Çinar, A. Bourdon, and T. Neubert, "Runaway electrons from a 'beam-bulk' model of streamer: Application to TGFs," Environ. Res. Lett. 9, 055003 (2014).
- <sup>15</sup>J. R. Dwyer, "Implications of x-ray emission from lightning," Geophys. Res. Lett. 31, L12102, https://doi.org/10.1029/2004GL019795 (2004).
- <sup>16</sup>S. Celestin and V. P. Pasko, "Energy and fluxes of thermal runaway electrons produced by exponential growth of streamers during the stepping of lightning leaders and in transient luminous events," J. Geophys. Res. 116, A03315, https://doi.org/10.1029/2010JA016260 (2011).
- 17 J. R. Dwyer, Z. Saleh, H. K. Rassoul, D. Concha, M. Rahman, V. Cooray, J. Jerauld, M. A. Uman, and V. A. Rakov, "A study of x-ray emission from laboratory sparks in air at atmospheric pressure," J. Geophys. Res. 113, D23207, https://doi.org/10.1029/2008JD010315 (2008).
- <sup>18</sup>M. J. Berger, M. Inokuti, H. H. Anderson, H. Bichsel, J. A. Dennis, D. Powers, S. M. Seltzer, and J. E. Turner, "ICRU Report 37: Stopping power for electrons and positrons," J. Int. Comm. Radiat. Units Meas. osl9, 1–176 (1982); available at <a href="https://www.govinfo.gov/content/pkg/GOVPUB-C13-139be796c7e56cb34375ad52db8ec5e7/pdf/GOVPUB-C13-139be796c7e56cb34375ad52db8ec5e7.pdf">https://www.govinfo.gov/content/pkg/GOVPUB-C13-139be796c7e56cb34375ad52db8ec5e7.pdf</a> (1984).
- <sup>19</sup>J. D. Jackson, "Charge density on thin straight wire, revisited," Am. J. Phys. 68, 789–799 (2000).
- <sup>20</sup>C. B. Moore, K. B. Eack, G. D. Aulich, and W. Rison, "Energetic radiation associated with lightning stepped-leaders," Geophys. Res. Lett. 28, 2141–2144, https://doi.org/10.1029/2001GL013140 (2001).
- <sup>21</sup>J. R. Dwyer, M. A. Uman, H. K. Rassoul, M. Al-Dayeh, L. Caraway, J. Jerauld, V. A. Rakov, D. M. Jordan, K. J. Rambo, V. Corbin, and B. Wright, "Energetic radiation produced during rocket-triggered lightning," Science 299, 694–697 (2003).
- <sup>22</sup>J. R. Dwyer, H. K. Rassoul, M. Al-Dayeh, L. Caraway, A. Chrest, B. Wright, E. Kozak, J. Jerauld, M. A. Uman, V. A. Rakov, D. M. Jordan, and K. J. Rambo, "X-ray bursts associated with leader steps in cloud-to-ground lightning," Geophys. Res. Lett. 32, L01803, https://doi.org/10.1029/2004GL021782 (2005).
- <sup>23</sup>J. Howard, M. A. Uman, J. R. Dwyer, D. Hill, C. Biagi, Z. Saleh, J. Jerauld, and H. K. Rassoul, "Co-location of lightning leader x-ray and electric field change sources," Geophys. Res. Lett. 35, L13817, https://doi.org/10.1029/2008GL034134 (2008).
- <sup>24</sup>J. R. Dwyer, M. Schaal, H. K. Rassoul, M. A. Uman, D. M. Jordan, and D. Hill, "High-speed x-ray images of triggered lightning dart leaders," J. Geophys. Res. 116, D20208, https://doi.org/10.1029/2011JD015973 (2011).
- 25M. M. Schaal, J. R. Dwyer, S. Arabshahi, E. S. Cramer, R. J. Lucia, N. Y. Liu, H. K. Rassoul, D. M. Smith, J. W. Matten, A. G. Reid, J. D. Hill, D. M. Jordan, and M. A. Uman, "The structure of x-ray emissions from triggered lightning leaders measured by a pinhole-type x-ray camera," J. Geophys. Res. 119, 982–1002, https://doi.org/10.1002/2013JD020266 (2014).
- <sup>26</sup>S. Frankel, V. Highland, T. Sloan, O. van Dyck, and W. Wales, "Observation of x-rays from spark discharges in a spark chamber," Nucl. Instrum. Methods 44, 345–348 (1966).
- 27Y. L. Stankevich and V. G. Kalinin, "Fast electrons and x-ray radiation during the initial stage of growth of a pulsed spark discharge in air," Sov. Phys. Dokl. 12, 1042–1043 (1967).

- <sup>28</sup>R. C. Noggle, E. P. Krider, and J. R. Wayland, "A search for x-rays from helium and air discharges at atmospheric pressure," J. Appl. Phys. 39, 4746 (1968).
- <sup>29</sup>L. V. Tarasova and L. N. Khudyakova, "X rays from pulsed discharges in air," Sov. Phys. Tech. Phys. 14, 1148 (1970).
- <sup>30</sup>J. R. Dwyer, H. K. Rassoul, Z. Saleh, M. A. Uman, J. Jerauld, and J. A. Plumer, "X-ray bursts produced by laboratory sparks in air," Geophys. Res. Lett. 32, L20809, https://doi.org/10.1029/2005GL024027 (2005).
- <sup>31</sup>I. D. Kostyrya, V. F. Tarasenko, A. N. Tkachev, and S. I. Yakovlenko, "X-ray radiation due to nanosecond volume discharges in air under atmospheric pressure," Tech. Phys. 51, 356–361 (2006).
- <sup>32</sup>C. V. Nguyen, A. P. J. van Deursen, and U. Ebert, "Multiple x-ray bursts from long discharges in air," J. Phys. D 41, 234012 (2008).
- <sup>33</sup>C. V. Nguyen, A. P. J. van Deursen, E. J. M. van Heesch, G. J. J. Winands, and A. J. M. Pemen, "X-ray emission in streamer-corona plasma," J. Phys. D 43, 025202 (2010).
- 34V. March and J. Montanyà, "Influence of the voltage-time derivative in x-ray emission from laboratory sparks," Geophys. Res. Lett. 37, L19801, https://doi.org/10.1029/2010GL044543 (2010).
- 35T. Shao, C. Zhang, Z. Niu, P. Yan, V. F. Tarasenko, E. K. Baksht, I. D. Kostyrya, and V. Shutko, "Runaway electron preionized diffuse discharges in atmospheric pressure air with a point-to-plane gap in repetitive pulsed mode," J. Appl. Phys. 109, 083306 (2011).
- <sup>36</sup>T. Shao, V. F. Tarasenko, C. Zhang, D. V. Rybka, I. D. Kostyrya, A. V. Kozyrev, P. Yan, and V. Y. Kozhevnikov, "Runaway electrons and x-rays from a corona discharge in atmospheric pressure air," New J. Phys. 13, 113035 (2011).
- <sup>37</sup>C. Zhang, T. Shao, V. F. Tarasenko, H. Ma, C. Ren, I. D. Kostyrya, D. Zhang, and P. Yan, "X-ray emission from a nanosecond-pulse discharge in an inhomogeneous electric field at atmospheric pressure," Phys. Plasmas 19, 123516 (2012).
- <sup>38</sup>P. O. Kochkin, C. V. Nguyen, A. P. J. van Deursen, and U. Ebert, "Experimental study of hard x-rays emitted from metre-scale positive discharges in air," J. Phys. D 45, 425202 (2012).
- <sup>39</sup>P. O. Kochkin, A. P. J. van Deursen, and U. Ebert, "Experimental study on hard x-rays emitted from metre-scale negative discharges in air," J. Phys. D 48, 025205 (2015).
- <sup>40</sup>V. Tarasenko, "Runaway electrons in diffuse gas discharges," Plasma Sources Sci. Technol. 29, 034001 (2020).
- <sup>41</sup>S. Agostinelli, J. Allison, K. Amako, J. Apostolakis, H. Araujo, P. Arce, M. Asai, D. Axen, S. Banerjee, G. Barrand, F. Behner, L. Bellagamba, J. Boudreau, L. Broglia, A. Brunengo, H. Burkhardt, S. Chauvie, J. Chuma, R. Chytracek, G. Cooperman, G. Cosmo, P. Degtyarenko, A. Dell'Acqua, G. Depaola, D. Dietrich, R. Enami, A. Feliciello, C. Ferguson, H. Fesefeldt, G. Folger, F. Foppiano, A. Forti, S. Garelli, S. Giani, R. Giannitrapani, D. Gibin, J. Gomez Cadenas, I. Gonzalez, G. Gracia Abril, G. Greeniaus, W. Greiner, V. Grichine, A. Grossheim, S. Guatelli, P. Gumplinger, R. Hamatsu, K. Hashimoto, H. Hasui, A. Heikkinen, A. Howard, V. Ivanchenko, A. Johnson, F. Jones, J. Kallenbach, N. Kanaya, M. Kawabata, Y. Kawabata, M. Kawaguti, S. Kelner, P. Kent, A. Kimura, T. Kodama, R. Kokoulin, M. Kossov, H. Kurashige, E. Lamanna, T. Lampen, V. Lara, V. Lefebure, F. Lei, M. Liendl, W. Lockman, F. Longo, S. Magni, M. Maire, E. Medernach, K. Minamimoto, P. M. de Freitas, Y. Morita, K. Murakami, M. Nagamatu, R. Nartallo, P. Nieminen, T. Nishimura, K. Ohtsubo, M. Okamura, S. O'Neale, Y. Oohata, K. Paech, J. Perl, A. Pfeiffer, M. Pia, F. Ranjard, A. Rybin, S. Sadilov, E. D. Salvo, G. Santin, T. Sasaki, N. Savvas, Y. Sawada, S. Scherer, S. Sei, V. Sirotenko, D. Smith, N. Starkov, H. Stoecker, J. Sulkimo, M. Takahata, S. Tanaka, E. Tcherniaev, E. S. Tehrani, M. Tropeano, P. Truscott, H. Uno, L. Urban, P. Urban, M. Verderi, A. Walkden, W. Wander, H. Weber, J. Wellisch, T. Wenaus, D. Williams, D. Wright, T. Yamada, H. Yoshida, and D. Zschiesche, "Geant4—A simulation toolkit," Nucl. Instrum. Methods Phys. Res., Sect. A 506, 250-303 (2003).

- <sup>42</sup>J. Allison, K. Amako, J. Apostolakis, H. Araujo, P. A. Dubois, M. Asai, G. Barrand, R. Capra, S. Chauvie, R. Chytracek, G. A. P. Cirrone, G. Cooperman, G. Cosmo, G. Cuttone, G. G. Daquino, M. Donszelmann, M. Dressel, G. Folger, F. Foppiano, J. Generowicz, V. Grichine, S. Guatelli, P. Gumplinger, A. Heikkinen, I. Hrivnacova, A. Howard, S. Incerti, V. Ivanchenko, T. Johnson, F. Jones, T. Koi, R. Kokoulin, M. Kossov, H. Kurashige, V. Lara, S. Larsson, F. Lei, O. Link, F. Longo, M. Maire, A. Mantero, B. Mascialino, I. McLaren, P. M. Lorenzo, K. Minamimoto, K. Murakami, P. Nieminen, L. Pandola, S. Parlati, L. Peralta, J. Perl, A. Pfeiffer, M. G. Pia, A. Ribon, P. Rodrigues, G. Russo, S. Sadilov, G. Santin, T. Sasaki, D. Smith, N. Starkov, S. Tanaka, E. Tcherniaev, B. Tome, A. Trindade, P. Truscott, L. Urban, M. Verderi, A. Walkden, J. P. Wellisch, D. C. Williams, D. Wright, and H. Yoshida, "Geant4 developments and applications," IEEE Trans. Nucl. Sci. 53, 270–278 (2006).
- 43 J. Allison, K. Amako, J. Apostolakis, P. Arce, M. Asai, T. Aso, E. Bagli, A. Bagulya, S. Banerjee, G. Barrand, B. Beck, A. Bogdanov, D. Brandt, J. Brown, H. Burkhardt, P. Canal, D. Cano-Ott, S. Chauvie, K. Cho, G. Cirrone, G. Cooperman, M. Cortes-Giraldo, G. Cosmo, G. Cuttone, G. Depaola, L. Desorgher, X. Dong, A. Dotti, V. Elvira, G. Folger, Z. Francis, A. Galoyan, L. Garnier, M. Gayer, K. Genser, V. Grichine, S. Guatelli, P. Gueye, P. Gumplinger, A. Howard, I. Hrivnacova, S. Hwang, S. Incerti, A. Ivanchenko, V. Ivanchenko, F. Jones, S. Jun, P. Kaitaniemi, N. Karakatsanis, M. Karamitros, M. Kelsey, A. Kimura, T. Koi, H. Kurashige, A. Lechner, S. Lee, F. Longo, M. Maire, D. Mancusi, A. Mantero, E. Mendoza, B. Morgan, K. Murakami, T. Nikitina, L. Pandola, P. Paprocki, J. Perl, I. Petrovic, M. Pia, W. Pokorski, J. Quesada, M. Raine, M. Reis, A. Ribon, A. Ristic Fira, F. Romano, G. Russo, G. Santin, T. Sasaki, D. Sawkey, J. Shin, I. Strakovsky, A. Taborda, S. Tanaka, B. Tome, T. Toshito, H. Tran, P. Truscott, L. Urban, V. Uzhinsky, J. Verbeke, M. Verderi, B. Wendt, H. Wenzel, D. Wright, D. Wright, T. Yamashita, J. Yarba, and H. Yoshida, "Recent developments in Geant4," Nucl. Instrum. Methods Phys. Res., Sect. A 835, 186-225 (2016).
- <sup>44</sup>A. B. Skeltved, N. Østgaard, B. Carlson, T. Gjesteland, and S. Celestin, "Modeling the relativistic runaway electron avalanche and the feedback mechanism with GEANT4," J. Geophys. Res. 119, 9174–9191, https://doi.org/ 10.1002/2014JA020504 (2014).
- <sup>45</sup>C. Rutjes, D. Sarria, A. B. Skeltved, A. Luque, G. Diniz, N. Østgaard, and U. Ebert, "Evaluation of Monte Carlo tools for high energy atmospheric physics," Geosci. Model Dev. 9, 3961–3974 (2016).
- <sup>46</sup>D. Sarria, C. Rutjes, G. Diniz, A. Luque, K. Ihaddadene, J. Dwyer, N. Østgaard, A. Skeltved, I. Ferreira, and U. Ebert, "Evaluation of Monte Carlo tools for high-energy atmospheric physics II: Relativistic runaway electron avalanches," Geosci. Model Dev. 11, 4515–4535 (2018).
- <sup>47</sup>Geant4Collaboration, Geant4 Installation Guide Documentation Release 10.4 (Geant4Collaboration, 2017).
- <sup>48</sup>B. E. Carlson, N. Østgaard, P. Kochkin, Ø. Grondahl, R. Nisi, K. Weber, Z. Scherrer, and K. LeCaptain, "Meter-scale spark x-ray spectrum statistics," J. Geophys. Res. 120, 11,191–11,202, https://doi.org/10.1002/2015JD023849 (2015).
- <sup>49</sup>C. Mooney and R. Duval, Bootstrapping: A Nonparametric Approach to Statistical Inference, Quantitative Applications in the Social Sciences (SAGE Publications, 1993).
- 50 F. H. Attix, Introduction to Radiological Physics and Radiation Dosimetry (John Wiley & Sons, 1986), p. 628.
- <sup>51</sup>L. P. Babich, High-Energy Phenomena in Electric Discharges in Dense Gases: Theory, Experiment, and Natural Phenomena (Futurepast Inc., 2003), p. 358.
- 52R. D. Evans, *The Atomic Nucleus* (McGraw-Hill, New York, 1955), p. 988.
- <sup>53</sup>See J. H. Hubbell and S. M. Seltzer, http://physics.nist.gov/xaamdi for "Tables of x-ray mass attenuation coefficients and mass energy-absorption coefficients (version 1.4)," [National Institute of Standards and Technology (NIST), Gaithersburg, MD, 2004], accessed 1 December 2018.
- 54 Saint-Gobain, Manual: Lanthanum Bromide Integrated Detector Design (Saint-Gobain Crystals, 2018).